

Spatial Deconvolution of Aerial Radiometric Survey and its application to the Fallout from a Radiological Dispersal Device

Laurel E. Sinclair, Richard Fortin

*Canadian Hazards Information Service, Natural Resources Canada, Ottawa, Ontario,
Canada*

Abstract

Mapping radioactive contamination using aerial survey measurements is an area under active investigation today. The radiometric aerial survey technique has been extensively applied following reactor accidents and also would provide a key tool for response to a malicious radiological or nuclear incident. Methods exist to calibrate the aerial survey system for quantification of the concentration of natural radionuclides, which can provide guidance. However, these methods have anticipated a spatial distribution of the source which is large in comparison to the survey altitude. In rapid emergency-response aerial surveys of areas of safety concern, deposits of relatively small spatial extent may be expected. The activity of such spatially restricted hot spots is underestimated using the traditional methods. We present here a spatial deconvolution method which can recover some of the variation smoothed out by the averaging due to survey at altitude. We show that the method can recover the true spatial distribution of concentration of a synthetic source. We then apply the method to real aerial survey data collected following detonation of a radiological dispersal device. The findings and implications of the deconvolution are then discussed by reference to a groundbased truckborne survey over the same contamination.

Keywords: aerial, airborne, mobile survey, unfolding, deconvolution, inversion, MINUIT, MINOS

1. Introduction

Aerial radiometric survey is a mature field. Successful prospecting for economically viable ore deposits using the radiation signal from naturally occurring rocks stretches back decades [1]. Survey systems composed of large volumes of NaI(Tl) scintillator gamma-ray detectors, as much as 20 L, coupled with georeferenced position sensors (now making use of the global navigation satellite system (GNSS)), record gamma energy spectra versus position. This information is later processed to produce maps of natural potassium, uranium and thorium concentrations. Standards exist to guide practitioners in this area [2, 3] and vast regions of the earth have been covered [4]. Practitioners have also developed methods to correct for terrain variation in aerial survey [5, 6].

The emphasis in aerial radiometric survey methods until recently has been on development of techniques suitable for geologic sources, for which the simplification of the source as an infinite and uniform sheet is reasonable in comparison with the distance scales of the survey parameters (altitude, line spacing). The higher an aircraft flies, the more that far-away locations contribute to the detected signal, relative to locations directly underneath the aircraft [7]. This can have the advantage of allowing for complete coverage in a more economical survey with wider line spacing. However, detection systems at higher altitude see a signal which is effectively averaged over a larger area of the ground. Anthropogenic signals such as those resulting in case of a reactor accident or malicious radiological dispersal could result in hot spots the concentration of which would be underestimated if averaged over a larger area.

In this paper, we present a method to deconvolve an aerial radiometric survey for spatial smearing. This kind of problem, requiring inversion of a spatial distribution, is encountered frequently in geophysical surveying. Geophysical spatial inversion problems are typically underdetermined, and one way of dealing with this has been to select only those solutions which are close to some preconceived model [8]. An approach to spatial deconvolution of airborne spectrometric data which relies on an analytical model for the response function, and allows underdetermined problems, has been published previously [9]. A related method for spatial inversion to the approach presented here, but using an iterative inversion and neglecting uncertainties, was published recently [10]. Other groups are taking a similar approach to that advocated here, but applied to the inversion of spectra rather than spatial

maps [11, 12].

The method which will be presented here was applied to data obtained using detectors aboard a manned helicopter. Nevertheless, it is prudent to mention the proliferation of work ongoing currently in aerial radiation detection from unmanned aerial vehicle (UAV) systems. The use of a UAV platform for aerial survey has facilitated the advance of aerial survey methodology. A good review of recent publications can be found here [13].

The method which will be presented here involves simply a) determining the influence of each independent region of the earth's surface on the measured spatial distribution and then b) optimizing the weight coefficients of each region of the surface to obtain the best reproduction of the measured map. The number of pixels of the solution can be chosen such that the problem is not underdetermined. No potentially biasing prior assumption about the underlying distribution is necessary. The method can handle complicated detector geometries as the response functions are determined in simulation. The method could easily be extended to allow it to be applied when there is significant terrain variation in the source such as would be the case in an urban environment. The method is stable under different starting conditions, and naturally allows for propagation of uncertainties from the measurement to the unfolded result.

We demonstrate the application of the unfolding method by applying it first to a synthetic data set. This is compared with the known underlying distribution. We proceed to apply the unfolding method to a real aerial survey measurement acquired following detonation of a radiological dispersal device [14].

This spatial deconvolution method has been presented previously at conferences by this group [15, 16], however, this is the first full write-up.

2. Methods

2.1. Unfolding method

A measurement of surface activity concentration under the uniform infinite plane assumption may be denoted $g^{\text{MEAS}}(x, y)$ where x and y represent easting and northing in geographic Cartesian coordinates. We seek to determine the true underlying surface radioactivity concentration, $f(x, y)$. $f(x, y)$ is related to $g^{\text{MEAS}}(x, y)$ through

$$g^{\text{MEAS}}(x, y) = S[f(x, y)], \quad (1)$$

where S represents the effect of the measurement system on $f(x, y)$.

We divide space into N^{PAR} pixels i , and using Monte Carlo simulation, generate uniform radioactivity distributions in each pixel, $f_i(x, y)$.

The measurement system S consists of the detection system as well as the air and all other absorbing and scattering materials between the source and the products of scattering, and the detectors. It is represented in the Monte Carlo simulation, and the emissions from the radioactive sources $f_i(x, y)$ are transported through the system S to obtain the template responses $g_i(x, y)$, where

$$g_i(x, y) = S[f_i(x, y)]. \quad (2)$$

We let

$$g(x, y) = \sum_{i=1}^{N^{\text{PAR}}} w_i g_i(x, y) \quad (3)$$

and fit $g(x, y)$ to $g^{\text{MEAS}}(x, y)$ using a χ^2 minimization [17] to extract the weighting coefficients w_i .

To examine this χ^2 function, let $g_j^{\text{MEAS}}(x, y)$ represent the j th measurement of the activity concentration $g^{\text{MEAS}}(x, y)$. Then

$$\chi^2 = \sum_{j=1}^{N^{\text{MEAS}}} \frac{g_j^{\text{MEAS}}(x, y) - \sum_{i=1}^{N^{\text{PAR}}} w_i g_i(x, y)}{e_j^2} \quad (4)$$

where there are N^{MEAS} measurements $g_j^{\text{MEAS}}(x, y)$ in the problem each with uncertainty e_j .

The estimator of $f(x, y)$ is then the reconstructed radioactivity concentration distribution $f^{\text{REC}}(x, y)$, where

$$f^{\text{REC}}(x, y) = \sum_{i=1}^{N^{\text{PAR}}} w_i f_i(x, y). \quad (5)$$

We choose to require the problem to be oversampled. That is, there is everywhere a greater spatial density of measurements than of fit parameters and $N^{\text{MEAS}} > N^{\text{PAR}}$. Then, provided that the uncertainties e_j in the denominator of the χ^2 function encompass all of the uncertainties of the problem, the minimum χ^2 value will be approximately equal to the number of degrees of freedom of the problem. And the MINOS algorithm [17] can be used to propagate the N^{MEAS} measurement uncertainties e_j through the fit procedure to calculate the N^{PAR} uncertainties δw_i on the weighting parameters

w_i . In practice, there are irreconcilable nonstochastic uncertainties affecting the problem which must be included in the e_j by application of a constant scaling factor to bring χ^2 per degree of freedom to one before the fit uncertainties can be utilized. These are due to the statistical uncertainties in the template responses $g_i(x, y)$, and the finite pixellization of the problem.

Uncertainties for spatial deconvolution of fallout surveys can be expected to be asymmetric owing to the boundary condition that the amount of deposition can not physically be less than zero. MINOS works by setting the positive and negative uncertainty for each parameter to the amount the parameter has to vary in each direction such that χ^2 increases by one. Thus MINOS naturally allows for asymmetric uncertainties and is particularly suited to uncertainty analysis in the measurement of amount of radioactivity.

2.2. Experimental method – aerial survey

The experimental methods to obtain the data to which we will apply the unfolding method have been described previously [14]. We will repeat only the most essential points here. Three RDD detonations were conducted during the trial. In the first, ~ 31 GBq of La-140 was dispersed explosively, with radioactive debris subsequently carried by wind as far as ~ 2 km from the site of the detonation. Aerial gamma-ray spectrometric surveys were conducted using two $10.2 \times 10.2 \times 40.6$ cm³ NaI(Tl) crystals mounted exterior to a helicopter in a skid-mounted cargo expansion basket. GNSS antennae and inertial navigation and altimetry systems were also installed in the basket, to determine location. The system recorded a linearized 1024-channel gamma-ray energy spectrum over the domain 0 MeV to 3 MeV, tagged with the location information, once per second. Post-acquisition, counts were selected from the spectra in an energy window of approximately four sigma in width around the 1.6 MeV La-140 photopeak. These count rates were corrected for lag and dead time. Count rates were also corrected for variations in flight altitude to the nominal flying height making use of the Shuttle Radar Topography Mission [18] digital terrain model adjusted to the local elevation using a GNSS base station. Backgrounds due to the radioactivity of the earth, the atmosphere, the aircraft and its occupants, and cosmic rays, were all subtracted. The count rates were all corrected for radioactive decay, back to the time of the blast. A coefficient to convert the measurements from counts per second to kBq/m², assuming an infinite and uniform source, was obtained from experimentally validated Monte Carlo simulation. Finally,

measurements of radioactivity concentration in kBq/m² for four aerial surveys, two conducted after the first blast and one conducted after each of the subsequent two blasts, were presented.

In this paper, we will discuss only the data recorded during the first aerial survey after the first blast. This survey was flown at a nominal 40 m flying height, with speed of 25 m/s and flight-line spacing of 50 m.

2.3. Experimental method – truckborne survey

2.3.1. Data collection – truckborne survey

Truckborne surveys were driven by criss-crossing the deposited fallout in an extemporaneous pattern following the first and third RDD blasts, restricting to the part of the fallout outside of a 500 m x 500 m fenced hot zone [19, 20]. The detection system was mounted in the bed of a pickup truck and consisted of four 10.2 x 10.2 x 40.6 cm³ NaI(Tl) crystals oriented vertically in a self-shielding arrangement for azimuthal direction measurement. Truckborne data following the first RDD blast will be presented here for comparison with the aerial survey data. The truckborne data has not undergone sufficient analysis for a full quantitative evaluation, but the shape will nevertheless provide an interesting comparison for interpretation of the aerial survey data.

2.3.2. Sensitivity calculation – truckborne survey

The sensitivity of the truckborne system to a La-140 contamination on the ground was determined using experimentally validated Monte Carlo simulation. In the simulations, the detector was placed with the centre of its sensitive volume at a height of 1.2 m above ground. The NaI(Tl) crystals and their housing were represented in the simulation in their vertical arrangement. The ~ 5000 kg of mass of the pick-up truck carrying the detector was represented by simple blocks of steel.

Sensitivity validation data was collected by placing a La-140 source of known emission rate at fixed locations around the truck and detector system. The dead material was adjusted in size and position in the model until an acceptable agreement with the sensitivity validation data was obtained. The engine and other materials at the front of the truck effectively block radiation coming from that direction, and most of the detected counts arise from radiation originating to the side and rear of the truck where there is comparatively little material. The uncertainty in the estimation of the sensitivity of the truckborne detector obtained in this manner is large, about

20% to 30%. This level of accuracy is sufficient for illumination of the value of the spatial deconvolution applied to the aerial data by comparison with data collected from a ground-based system.

Fig. 1 a) shows the number of energy deposits registered in the detector per second as a function of the radius R of a disc-shaped source centered beneath the truckborne detector on the ground as determined by the simulation. The expression for the flux, $\Phi(R, H)$, due to a surface activity concentration

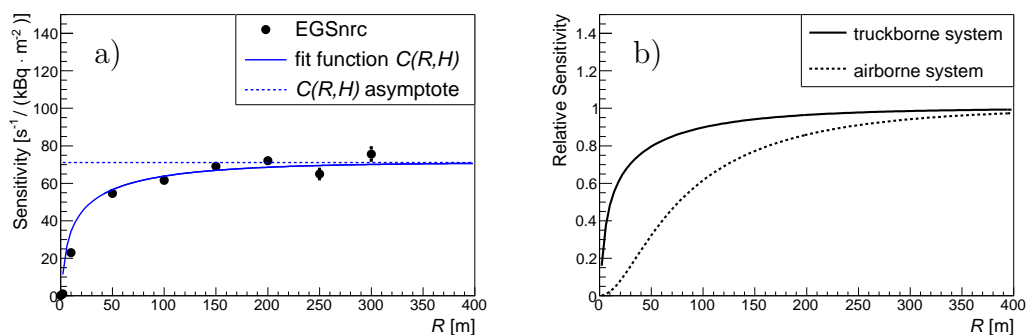


Figure 1: a) Sensitivity of the truckborne survey system to a disc-shaped distribution of isotropic emitters of the La-140 gamma spectrum, as a function of disk radius. Black dots show EGSnrc prediction. Solid curve shows fit of the expression $C(R, H)$ to the synthetic data. The dashed line shows the asymptote of the fit curve and represents the sensitivity to a uniform and infinite sheet source. b) Comparison of the shapes of the sensitivity curves for the aerial and truckborne survey systems. The dashed line shows the sensitivity to a disc source relative to the sensitivity to an infinite sheet as a function of disc radius for an aerial survey system at an altitude of 40 m [14]. The solid line shows the equivalent relative sensitivity curve for the truckborne survey system.

S_0 at a point an elevation H above a disc-shaped source of radius R can be readily calculated [7],

$$\Phi(R, H) = \frac{S_0}{2} (E_1(\mu_a H) - E_1(\mu_a \sqrt{H^2 + R^2})), \quad (6)$$

where E_1 is the exponential integral and μ_a is the linear attenuation coefficient for gamma rays in air. To determine the asymptotic sensitivity, we formed a function for the detected counts as a function of the source radius,

$$C(R, H) = \epsilon \Phi(R, H), \quad (7)$$

and fit the expression for $C(R, H)$ to the synthetic data to obtain the detection efficiency ϵ . The fit result is shown as the solid curve in Fig. 1a) and the asymptotic sensitivity, shown by the dashed line, is $\sim 71 \text{ s}^{-1}/(\text{kBq}/\text{m}^2)$. As mentioned, the uncertainty on this sensitivity is large due to the lack of detailed representation of the shielding material of the truck in the simulation. Nevertheless, the shape of the sensitivity curve is of value, as is the shape of the profile of counts measured with the truckborne system as it traversed the deposited plume.

2.3.3. Comparison of aerial and truckborne sensitivity curves

Fig. 1b) shows a comparison of the shapes of the sensitivity curves of the ground-based and aerial systems. Despite the tall narrow shape of its detectors, which would tend to increase sensitivity to incoming radiation from the sides, for the truckborne system at “altitude” $H = 1.2 \text{ m}$, a greater percentage of detected gamma rays originate close to the point directly underneath the detector as compared to the airborne system at $H = 40 \text{ m}$. This leads to superior spatial precision in the results of truckborne survey.

2.4. Aerial survey template response determination through Monte Carlo simulation

The radiation transport model EGSnrc [21, 22] was used to generate the individual uniform pixel sources $f_i(x, y)$ and to propagate the generated gamma rays and their interaction products through air and into the detection volume to create the template responses $g_i(x, y)$. For the solutions presented herein, the simulation geometry represented the experimental setup during the first RDD trial [14]. The actual aerial survey system was described and shown in photographs in the previous publication and briefly reiterated in Sect. 2.2. The model of that system in EGSnrc is shown in Fig. 2 a). The simulated gamma detection system included the two NaI(Tl) crystals, as well as their aluminum cladding, and felt, foam and carbon fibre enclosure. The exterior-mounted basket containing the detectors was modelled in a simplified manner with 51 3 mm x 1.5 mm bars of aluminum, representing the basket strands, running the length of the basket in a semicircle around its long axis. Dead materials due to the photo-multiplier tube readout of the crystals and associated electronics, as well as the altimeter and GNSS receivers, were modelled as simple blocks of metal of the appropriate overall mass. The ground was represented as perfectly flat with the detection system at a height of 40 m. The model was validated experimentally using data

from point sources of known emission rate placed at known locations around the actual detector. The uncertainty associated with approximation in the representation of the measurement system in the model was evaluated by variation of the arrangement of dead material in the model, by variation of the detector’s position, altitude and attitude and by variation of the detector’s energy resolution within reasonable limits. This uncertainty was evaluated to be about 12% on the activity concentration and it was included the overall systematic uncertainty quoted in th

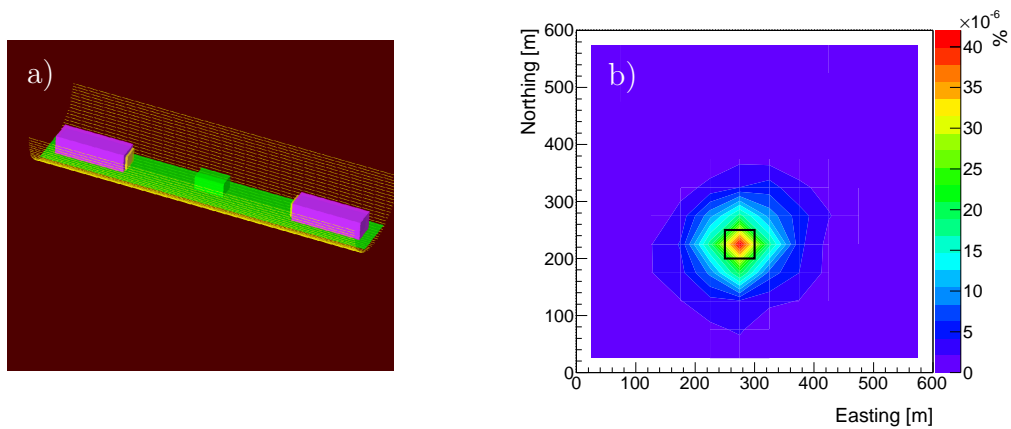


Figure 2: a) The aerial survey system as modelled in EGSnrc. The two $10.2 \times 10.2 \times 40.6 \text{ cm}^3$ NaI(Tl) crystals are represented in their housing, shown in purple, with steel blocks at the ends representing the dead material of the PMTs and readout electronics. The two crystals are mounted lengthwise with their centres 152.4 cm apart on an aluminium plate which is represented with mass and dimensions according to the engineering drawing. Auxilliary instrumentation is represented by an aluminium block in the centre of the basket, of the summed instrument mass. This dead material is shown in green in the figure. The aluminum plate on which the detectors and auxiliary equipment is mounted is itself attached to a basket which is mounted to the skids on the outside of the helicopter. Dead material of the basket is represented by 51 thin aluminum bars running the length of the basket, in a semicircle around the basket long axis, shown in gold. Uncertainty on the sensitivities due to misrepresentation of the system in the model has been estimated to be approximately 12%. b) Response function, $g_{53}(x, y)$ to the pixel source $f_{53}(x, y)$, normalized to the number of generated events, where the x -axis shows Easting and the y -axis shows Northing. The true spatial extent of pixel 53 is indicated by the black square.

The simulated pixel sources, $f_i(x, y)$, consisted of uniform distributions of isotropic emitters of the La-140 spectrum of gamma rays, including all emis-

sion energies above 0.05% emission probability [23]. Gammas were emitted into the full 4π solid angle. Each pixel source $f_i(x, y)$ was square, and 50 m on a side. Note that with the survey parameters mentioned previously, we have one spectrum recorded approximately every 25 m x 50 m in the real data. Thus, the number of measurements in the data is higher than the number of fit parameters in the simulation, the problem is over-determined, and we can expect reasonably rapid convergence of the method to a solution which is stable under different starting conditions.

The entire region to be unfolded measured 1.5 km x 1.5 km. To speed up convergence of the fitting, we chose to parallelize the computation, breaking the problem up into individual tiles, each 500 m x 500 m. Only eight of these tiles were necessary to cover the area over which the radioactivity actually settled. To knit the tiles together, we extended the fit into a border of pixel sources 50 m wide, surrounding each tile. Thus the fit area corresponding to each tile was actually 600 m x 600 m. If, after background subtractions, fewer than one count corresponding to a La-140 energy deposit was measured in the detection system in the region of space corresponding to one fit parameter w_i , then that fit parameter was assigned a value of zero and left out of the minimization. Thus, 144 or fewer fit parameters w_i were determined from the inversion of each tile. To merge the tiles after the individual inversions, the weighting parameters of the border pixels were simply ignored, and the central 500 m x 500 m areas of the tiles were placed next to each other.

The simulation included one detection system for each of the 144 pixel sources, centered laterally within the pixel, at 40 m height. Here we have used multiple detection systems at different places at one time to represent the real world in which one detection system was in different places at different times. Given the 40 m height of the detection systems above the source, the 50 m spacing between them and the requirement that the deposited energy lie in the highest-energy photopeak of the source, the error in this approximation, which would come from a single emitted gamma ray depositing energy in two different detection systems, is negligible.

The volume of the air in which the gamma rays and electrons were tracked in each tile extended 1.2 km in easting (or x) and northing (or y), and 600 m up. A 5 m-thick concrete slab underneath the emitters and filling the lateral dimensions of the simulated volume, represented the earth.

The simulation included all physical interactions of the emitted gammas and of the gammas, electrons and positrons resulting from those interactions. Scattering and absorption in the air and “earth” of the simulated volume,

and in the dead material of the basket system and housing of the NaI(Tl) crystals, was included. All processes leading to energy deposit within the NaI(Tl) crystal from either the direct gamma rays, or the products of scattering, were included. Energy deposits in the NaI(Tl) were then smeared to create simulated spectra, according to the energy resolutions of the crystals determined during the experiment.

Fig. 2 b) shows the response, $g_{53}(x, y)$, of the 144 detection systems of one tile, as a percentage of the number of events generated in a single one of the pixel sources, $f_{53}(x, y)$, where this happens to correspond to the pixel numbered “53”. The extent of the source is indicated by the black square. Note how the measured response extends much more broadly in space. This is the spatial smearing which will be corrected by the unfolding.

3. Results

3.1. Results obtained by application of the method to synthetic data

We begin by applying the spatial inversion method to a synthetic data set for which we know the underlying distribution $f(x, y)$. An annular region consisting of the area between two circles of radius 100 m and 250 m, centered at (550 m, 550 m) was uniformly populated with $10 \cdot 10^9$ emitters of the La-140 gamma spectrum. Considering the branching ratios for the La-140 gamma emissions, this amounts to a source concentration of 28.4 kBq/m². The annular region is indicated by the black outlines in Fig.’s 3 a) and b).

Generation of the synthetic dataset makes use of the identical detector simulations as used in generating the template responses $g_i(x, y)$ as described in Section 2.4, however the detection systems were more narrowly spaced in the synthetic dataset. Detection systems for the synthetic dataset were located every 20 m in x and y such that there were 225 detection systems in total in each 600 m x 600 m tile.

The template sources $f_i(x, y)$ and the template responses $g_i(x, y)$ utilized in the inversion are the same as will be used for the real data and are as described in Section 2.4. Thus, the synthetic data measurement density of 20 m x 20 m exceeds the density of the parametrization, 25 m x 25 m, and the problem is overdetermined, as desired.

Fig. 3 a) shows the synthetic aerial survey measurement. The result is broader than the underlying true source distribution. Contamination appears to extend outside of the known true underlying borders. The central area of the annulus appears to be filled with significant contamination. The average

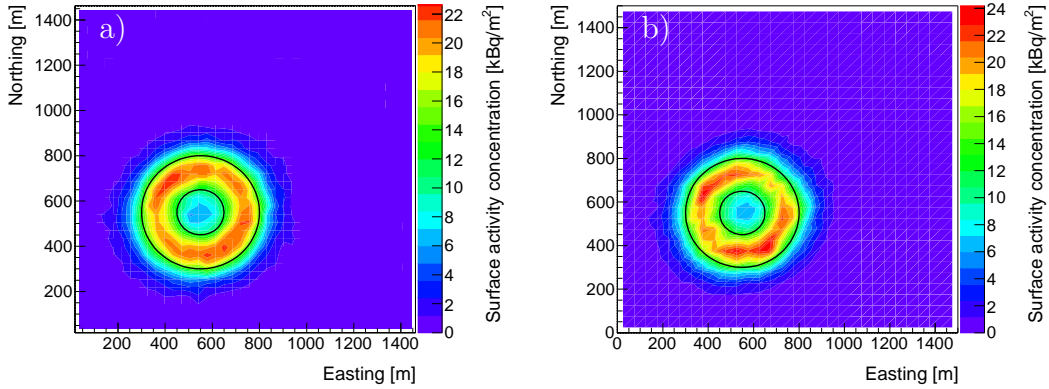


Figure 3: Synthetic aerial survey and fit results, where the x axis is Easting, and the y axis is Northing. The source was of concentration 28.4 kBq/m^2 and annular with inner radius 100 m and outer radius 250 m , centered at $(550 \text{ m}, 550 \text{ m})$, as indicated by the area between the black circles. a) Synthetic aerial survey measurement result. b) Result of fit of template responses $g_i(x, y)$ to the synthetic aerial survey.

concentration of contamination reconstructed within the annular region is lower than the known true concentration.

Fig. 3 b) shows the result of the fit of the template measured activity distributions to the synthetic aerial survey measurement. The colour scale used in Fig. 3 b) is the same as that of Fig. 3 a). The first observation to note is that the tile knitting procedure apparently works well. The synthetic data stretches over six of the overlapping $600 \text{ m} \times 600 \text{ m}$ simulation tiles. After knitting of the inverted result into adjacent non-overlapping $500 \text{ m} \times 500 \text{ m}$ tiles, there is seamless matching of the reconstructed activity concentration at the tile borders. Also to note is that within the limitations of the somewhat coarse pixellization of the problem, the survey is well reproduced by the fit. The tendency of the measurement to extend outside of the bounds of the true source is reproduced, as is the tendency of the measurement to underestimate the magnitude of the concentration within the source boundary.

The reconstruction of the true underlying source distribution for the synthetic data is presented in Fig. 4. As shown in Fig. 4 a), the inversion process results in a reconstructed source distribution which is higher in magnitude and closer to the true activity concentration than the initial survey measurement. The boundaries of the actual source are better reproduced after inversion, in particular the absence of radioactivity in the centre of the

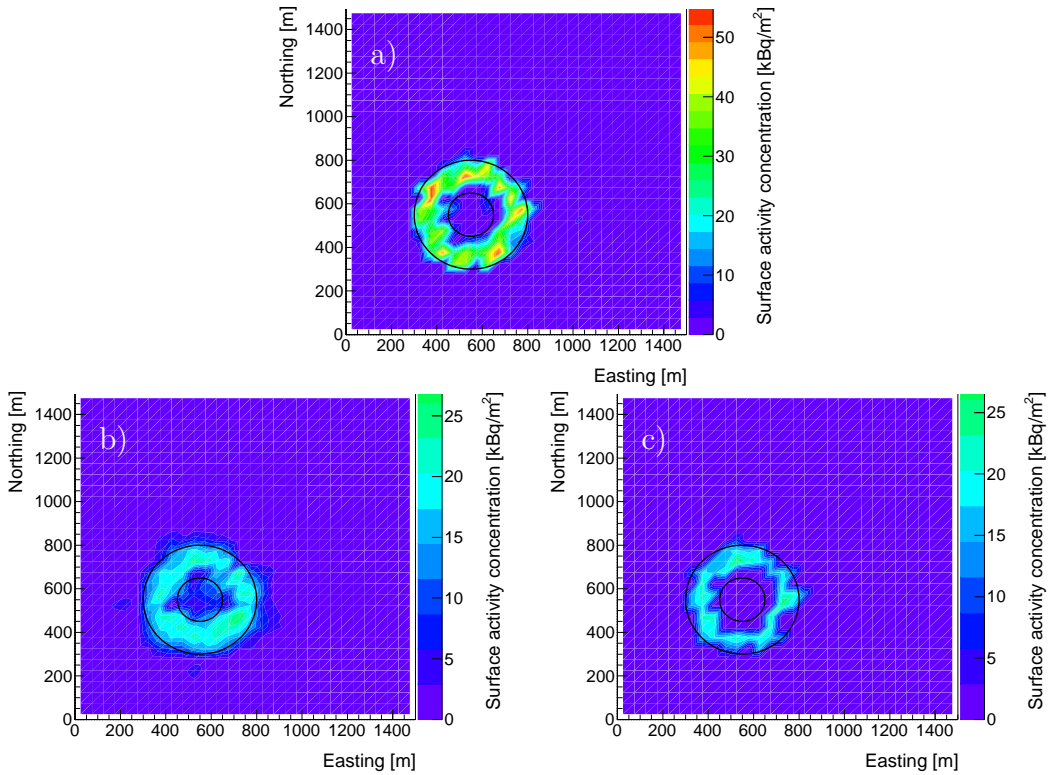


Figure 4: Spatially deconvolved synthetic aerial survey result, x axis is Easting and y axis is Northing. Black circles indicate the true annular source distribution. a) The spatially deconvolved measurement. b) Positive statistical uncertainty on the spatially deconvolved measurement. c) Negative statistical uncertainty on the spatially deconvolved measurement.

annulus is recovered.

A major advantage of the spatial deconvolution method presented here is that statistical uncertainties affecting the measurement may be propagated through the minimization procedure by the MINOS algorithm as described in Sect. 2.1. A map showing the one-sigma positive statistical uncertainty on the reconstructed surface activity concentration is shown in Fig. 4 b) and the corresponding negative statistical uncertainty is shown in Fig. 4 c) where the same colour scale is used for the uncertainties as for the measurement shown in Fig. 4 a). Considering the uncertainties, the ability of the method to reconstruct the true underlying activity concentration is good. The reconstructed activity concentration magnitude is in agreement with the known true activ-

ity concentration within uncertainties in most places. For example, near the inner boundary of the annulus where the reconstructed concentration is low compared to the known true concentration, further negative movement of the result is not allowed by the negative uncertainty. The positive uncertainty exceeds the negative uncertainty in magnitude, and does allow for a positive movement of the reconstructed value.

3.2. Real data collected following detonation of a radiological dispersal device

3.2.1. Spatial deconvolution of aerial survey data

The aerial survey measurement from the first RDD trial is shown in Fig. 5 a). This result has been published previously [14] and the meth-

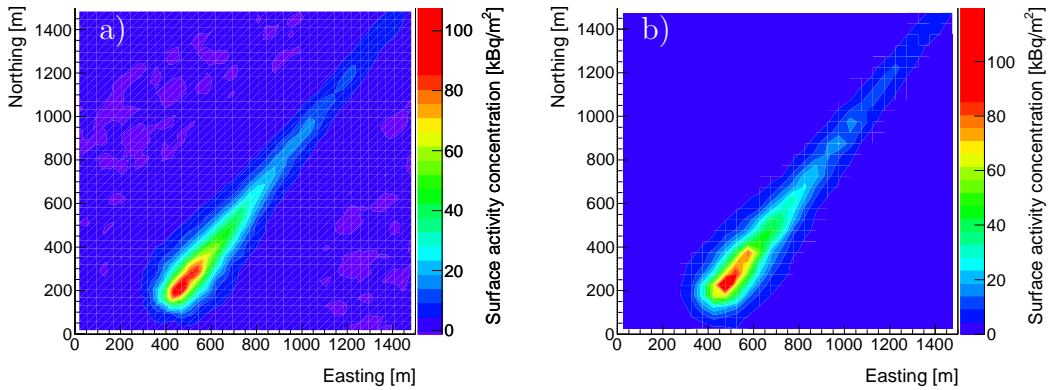


Figure 5: a) Aerial survey measurement of the distribution of fallout following detonation of the radiological dispersal device. b) Result of fit of template histograms to the aerial survey measurement.

ods to arrive at the result were recapitulated here in Sect. 2.2. We observe an area of activity concentration exceeding 100 kBq/m^2 near ground zero of the detonation, with a long deposited plume of maximum width of 300 m to 400 m, and significant measured radioactivity extending over a distance of about 2 km. The total systematic uncertainty affecting this measurement was determined to be around 12% and the statistical uncertainty peaks at 6 kBq/m^2 .

Fig. 5 b) shows the result of the χ^2 fit of the weighting coefficients of the template response functions to the measurement of Fig. 5 a). The colour scales of Fig.'s 5 a) and b) have been chosen to be equal. (This colour scale has in fact been set to the optimal colour scale for the data from a truckborne

survey which will be presented in the upcoming Sect. 3.2.2.) The features of the measurement are broadly well-reproduced by the fit, considering the pixellization of the reconstruction. In particular, the magnitude, width and extent of the contamination are well represented in the result of the fit.

The underlying distribution of pixel sources which gives rise to the fit result of Fig. 5 b) is presented in Fig. 6 a). This is the reconstructed distri-

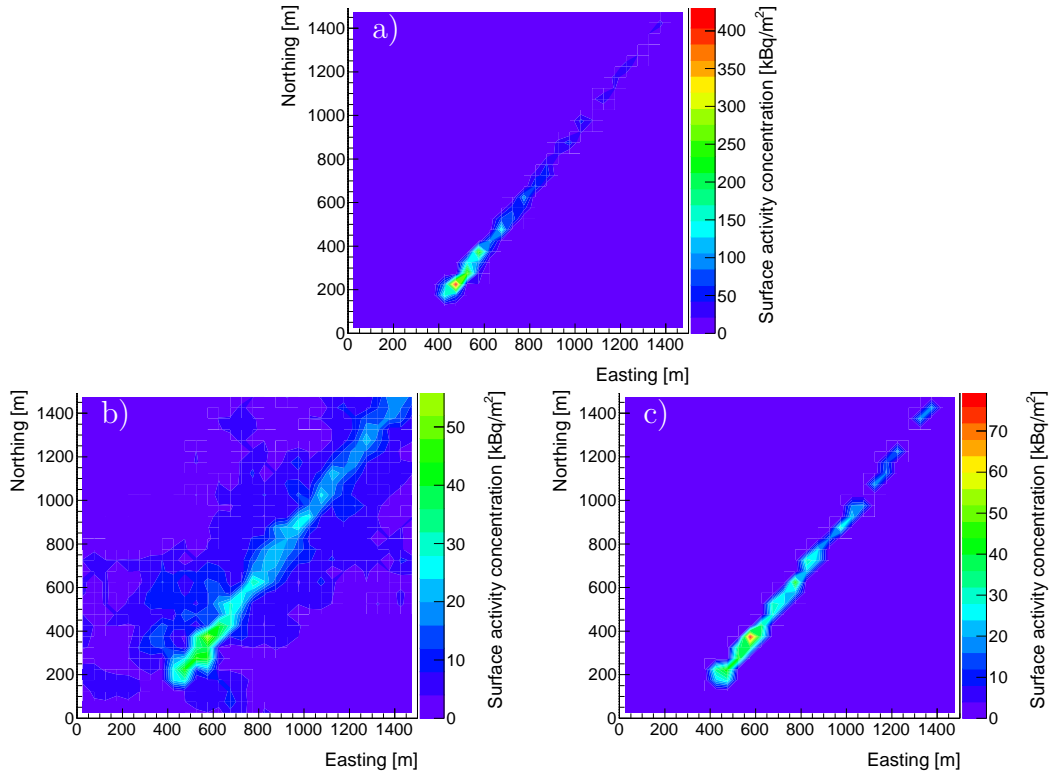


Figure 6: a) Spatially deconvolved aerial survey measurement of fallout following radiological dispersal device blast. b) Positive statistical uncertainty on spatially deconvolved measurement. c) Negative statistical uncertainty on spatially deconvolved measurement.

bution of the surface activity concentration following spatial deconvolution. We find that the width of the deposited plume is now much smaller than the original undeconvolved measurement, around 50 m. Correspondingly, the peak concentration is higher, over 400 kBq/m². Note that the width of the deposited plume is small with respect to the altitude and line spacing of the survey. This accounts for its significant overestimation when the

“infinite and uniform” approximation was used to obtain a concentration measurement from the measured counts as shown in Fig. 5 a) and [14]. The length of the deposition is however much larger than the survey parameters, so in this dimension the “infinite and uniform” sheet approximation is not so bad and the original length measurement is not much altered by the spatial deconvolution.

The positive and negative statistical uncertainties on the spatially deconvolved deposited fallout map are shown in Fig.’s 6 b) and c) respectively. Note that the statistical uncertainties affecting the measurement are very small, and on the colour scale of Fig. 6 a) would be difficult to see, so the colour scale in Fig.’s 6 b) and c) is chosen to optimize the representation of the information in Fig. 6 c). The uncertainties reveal important features of the measurement and its inversion. The positive uncertainty indicates a region extending away from the measured deposited plume axis in which a positive quantity of activity is permitted, however at a very low amount of between 5 kBq/m^2 and 10 kBq/m^2 . The negative uncertainty shows that the measurement of the presence and distribution of radioactivity is significantly above zero.

The MINOS error propagation includes only the stochastic uncertainties on the measurement. There are additional uncertainties which are systematic and arise from approximations in the representation of the system in the simulation. These include mis-representation of the position, particularly the altitude; the attitude (yaw, pitch and roll); the amount of shielding material in the basket containing the detectors; the energy resolution and the air density. The systematic uncertainty on the (undeconvolved) radioactivity concentration distribution was determined to be about 12% by variation of these parameters within reasonable limits [14].

For the spatially deconvolved measurement, some of the systematic uncertainties must be re-examined as they can be expected to have an effect on the shape of the reconstructed fallout distribution, as well as its overall magnitude. These are the systematic uncertainties associated with the measurement of altitude and pitch angle. It is also interesting to examine the effect of the measurement of yaw angle on the spatially inverted measurement as it can have no effect at all on the original undeconvolved measurement which used the infinite sheet approximation for the source and therefore the detector response was invariant under changes of yaw.

The inertial navigation system determined the yaw angle during the measurement to be around -30° . The spatial inversion was conducted twice. For

the central value of the inversion as presented in Fig. 6 a) the helicopter systems in the template histograms were assigned a yaw of -30° to match the data. To allow for changes in yaw during flight, the regression was repeated with yaw set maximally different at 60° . Pitch was varied from the nominal 0° to -10° according to the maximum deviation of pitch recorded by the inertial navigation system while on line during one sortie. Altitude was varied from nominal by 1 m to account for approximately one sigma of variability in height determination. These variations did not significantly alter the measurement of length and width of the deposited fallout. Added in quadrature, and considering that some of the variation was already included in the original systematic uncertainty associated with the sensitivity, the deviations do not yield a significant additional systematic uncertainty. Although not a significant additional source of uncertainty for the measurements presented here, these sources of uncertainty are worth discussing for the benefit of researchers following this approach under different operating conditions.

3.2.2. Comparison of spatially deconvolved aerial survey data with truckborne survey data

In Fig. 7a) the truckborne survey result which followed the first blast is shown overlaid on the undeconvolved aerial survey result from the same blast on the same colour scale. (The colour scale is optimized to show the variation in the truckborne survey result.) The truckborne survey reports much higher surface activity concentrations than the aerial survey and the fallout appears to be narrower in width.

Fig. 7b) shows the same truckborne survey result this time overlaid on the spatially deconvolved aerial survey measurement. (The colour scale is the same as that used in Fig. 7a).) Here, both the width and magnitude of the concentration are in better agreement.

The aerial survey maps were sampled at the locations of the truck and these sampled activity concentration values are presented in Fig. 7c) (top) as a function of the distance from the start of the truck-driven sortie. Again, it is clear that the spatially deconvolved result is generally higher at maximum magnitude and more narrow than the undeconvolved aerial survey result. The bottom part of Fig. 7c) shows the root-mean-square deviation (RMSD) of the curves calculated by sampling each profile at regular intervals from the maximum concentration down to the point at which the concentration falls below 10% of the maximum. This plot shows that the RMSD width of the

deposition according to the undeconvolved survey is typically around 90 m while the width of the deposition according to the truckborne survey and the spatially deconvolved aerial survey tends to be significantly narrower, closer to 30 m. Spatially deconvolved aerial survey thus recovers the narrowness of the fallout to approximately the same spectral precision as the truckborne survey.

Truckborne data is shown for the purpose of shape comparison only and does not include detailed error analysis. In any event, the truckborne system has its own finite area of sensitivity largely caused by its “altitude” of just over one metre, causing smearing of the measured spatial distribution. A contact measurement of the deposited radioactivity can be expected to be even more concentrated in places [24].

4. Discussion and Conclusions

Radiometric survey would be performed to map fallout following a reactor accident or following a malicious release. To cover a large area quickly, the surveys are initially performed using manned aircraft at some significant altitude H . If there is spatial variability in the fallout at distance scales much less than H , then the map result of the survey can underestimate the quantity of radioactivity on the ground in places.

We have presented here a method to deconvolve an aerial survey map for the spatial smearing caused by measurement at altitude, at least to the extent permitted by the sampling density as determined by the aircraft speed and line spacing. Performed on synthetic data, the deconvolution method returns a distribution which is consistent with the true underlying distribution within measurement uncertainty. The deconvolved distribution is more narrowly distributed, and shows regions of locally higher radioactivity concentration than the initial undeconvolved measurement. Performed on real data acquired following detonation of a radiological dispersal device, the method produces a distribution which is narrower and shows radioactivity concentration as much as four times that of the original measurement.

The method can unfold a distribution for smearing effects up to a resolution permittable by the sampling frequency of the original measurement. The method allows for propagation of stochastic measurement uncertainties through the unfolding to obtain the measurement uncertainties on the fit parameters. The method relies on application of the MINUIT and MINOS algorithms well known in the field of particle physics. What is perhaps not

well known is that these algorithms can tolerate operating with hundreds of independent fit parameters, converging to a stable solution in a reasonable amount of time from an arbitrary starting distribution. Our current need was to develop a method to extract the greatest possible information from a set of aerial surveys performed to improve scientific understanding of the behaviour of radiological dispersal devices. The method, however, is also applicable to unfolding of any smeared distribution of any dimensionality. It could find application in other fields.

The result of the unfolding is limited in spatial resolution by the requirement that the density of pixellization of the answer not exceed the density of measurements as determined by the aircraft speed and line spacing. Nevertheless, aerial survey practitioners should be aware that there is improved information about the spatial distribution of the radioactivity contained in their aerial survey map that can be extracted provided good knowledge of the response function of the system is available. The achieved spatial resolution for the particular aerial survey following RDD detonation presented here approximately matched that obtained during truckborne survey over the same deposition (while providing complete coverage). Contact measurements ($H = 0$ m) can be expected to reveal even greater local spatial variations than the truckborne data. Still, the truckborne survey “height” of about 1.2 m provides a salient benchmark for spatial resolution as this is close to the average height of an adult human. Should humans be required to enter a possibly contaminated area guided by the results of aerial survey alone, a spatially deconvolved aerial survey map could provide a better predictor of the activity concentrations they will encounter than the undeconvolved measurement.

Acknowledgements

The authors gratefully acknowledge the leadership of the RDD field trials under L. Erhardt, and helpful comments on the analysis from H.C.J. Seywerd, P.R.B. Saull and F.A. Marshall. Funding for this project was provided through Canada’s Chemical, Biological, Radiological-Nuclear and Explosives Research and Technology Initiative. This report is NRCan Contribution 20180112.

References

- [1] R. L. Grasty, Uranium measurement by airborne gamma-ray spectrometry, *Geophysics* 40 (1975) 503.
- [2] Airborne gamma ray spectrometer surveying, IAEA Technical Reports Series 323 (1991).
- [3] R. L. Grasty, Environmental monitoring by airborne gamma ray spectrometry, experience at the Geological Survey of Canada, Application of uranium exploration data and techniques in environmental studies, IAEA-TECDOC-827 (1995).
- [4] Radioelement Mapping, IAEA Nuclear Energy Series No. NF-T-1.3 (2010).
- [5] G. Schwarz, E. Klingele, L. Rybach, How to handle rugged topography in airborne gamma-ray spectrometry surveys, *First Break* 10 (1992) 11 – 17.
- [6] A. Ishizaki, Y. Sanada, M. Ishida, M. Munakata, Application of topographical source model for air dose rates conversions in aerial radiation monitoring, *J. Environ. Radioactiv.* 180 (2017) 82 – 89.
- [7] L. V. King, Absorption problems in radioactivity, *Phil. Mag.* 23 (1912) 242–250.
- [8] R. L. Parker, "Geophysical Inverse Theory", "Princeton University Press", "41 William St., Princeton, New Jersey 08540, USA", "2015".
- [9] B. Minty, R. Brodie, The 3D inversion of airborne gamma-ray spectrometric data, *Exploration Geophysics* 47 (2016) 150 – 157.
- [10] R. D. Penny, T. M. Crowley, B. M. Gardner, M. J. Mandell, Y. Guo, E. B. Haas, D. J. Knize, R. A. Kuharski, D. Ranta, R. Shyffer, S. Labov, K. Nelson, B. Seilhan, J. D. Valentine, Improved radiological/nuclear source localization in variable NORM background: An MLEM approach with segmentation data, *Nucl. Instr. and Meth. A* 784 (2015) 319 – 325.
- [11] J. Mattingly, D. J. Mitchell, A framework for the solution of inverse radiation transport problems, *IEEE Trans. Nucl. Sci.* 57 (6) (2010) 3734 – 3743.

- [12] E. M. A. Hussein, The physical and mathematical aspects of inverse problems in radiation detection and applications, *Appl. Radiat. Isot.* 70 (2012) 1131 – 1135.
- [13] D. Connor, P. G. Martin, T. B. Scott, Airborne radiation mapping: overview and application of current and future aerial systems, *Int. J. Remote Sens.* 37 (2016) 5953 – 5987.
- [14] L. Sinclair, R. Fortin, J. Buckle, M. Coyle, R. Van Brabant, B. Harvey, H. Seywerd, M. McCurdy, Aerial Mobile Radiation Survey Following Detonation of a Radiological Dispersal Device, *Health Phys.* 110 (2016) 458 – 470.
- [15] L. Sinclair, R. Fortin, Spatial Deconvolution of Aerial Radiometric Survey Results, CTBT: Science and Technology Conference, Presentation T3.2-P20, Vienna, Austria, accessed: March 23, 2018 (2015).
URL http://www.ctbto.org/fileadmin/user_upload/SnT2015/SnT2015_Posters/T3.2-P20
- [16] L. E. Sinclair, F. A. Marshall, R. Fortin, Reconstruction of the spatial distribution of radioactive contamination from aerial survey and from a stationary array of directional detectors, in: 2015 IEEE Nuclear Science Symposium and Medical Imaging Conference (NSS/MIC), 2015, pp. 1–4. doi:10.1109/NSSMIC.2015.7581989.
- [17] F. James, M. Roos, Minuit: A system for function minimization and analysis of the parameter errors and correlations, *Comput. Phys. Commun.* 10 (1975) 343–367. doi:10.1016/0010-4655(75)90039-9.
- [18] T. G. Farr, P. A. Rosen, E. Caro, R. Crippen, R. Duren, S. Hensley, M. Kobrick, M. Paller, E. Rodriguez, L. Roth, D. Seal, S. Shaffer, J. Shimada, J. Umland, M. Werner, M. Oskin, D. Burbank, D. Alsdorf, The shuttle radar topography mission, *Rev. Geophys.* 45 (2007) –.
URL <http://dx.doi.org/10.1029/2005RG000183>
- [19] A. Green, L. Erhardt, L. Lebel, M. Duke, T. Jones, D. White, D. Quayle, Overview of the Full-scale Radiological Dispersal Device Field Trials, *Health Phys.* 110 (2016) 403 – 417.
- [20] F. Marshall, Reconstruction of the Spatial Distribution of Surface Activity Concentration for an In-Situ, Gamma-Ray, Truck-borne Survey , Master’s thesis, Carleton University, Canada (2014).

- [21] I. Kawrakow, E. Mainegra-Hing, D. W. O. Rogers, F. Tessier, B. R. B. Walters, The EGSnrc Code System, NRC Report PIRS-701 (2011).
- [22] I. Kawrakow, E. Mainegra-Hing, F. Tessier, B. R. B. Walters, The EGSnrc C++ class library, NRC Report PIRS-898 (2011).
- [23] M.-M. Bé, V. Chisté, C. Dulieu, E. Browne, V. Chechev, N. Kuzmenko, R. Helmer, A. Nichols, E. Schönfeld, R. Dersch, Table of Radionuclides, Vol. 1 of Monographie BIPM-5, Bureau International des Poids et Mesures, Pavillon de Breteuil, F-92310 Sèvres, France, 2004.
- [24] L. Erhardt, L. Lebel, E. Korpach, R. Berg, E. Inrig, I. Watson, C. Liu, C. Gilhuly, D. Quayle, Deposition Measurements from the Full-Scale Radiological Dispersal Device Field Trials, *Health Phys.* 110 (2016) 442 – 457.

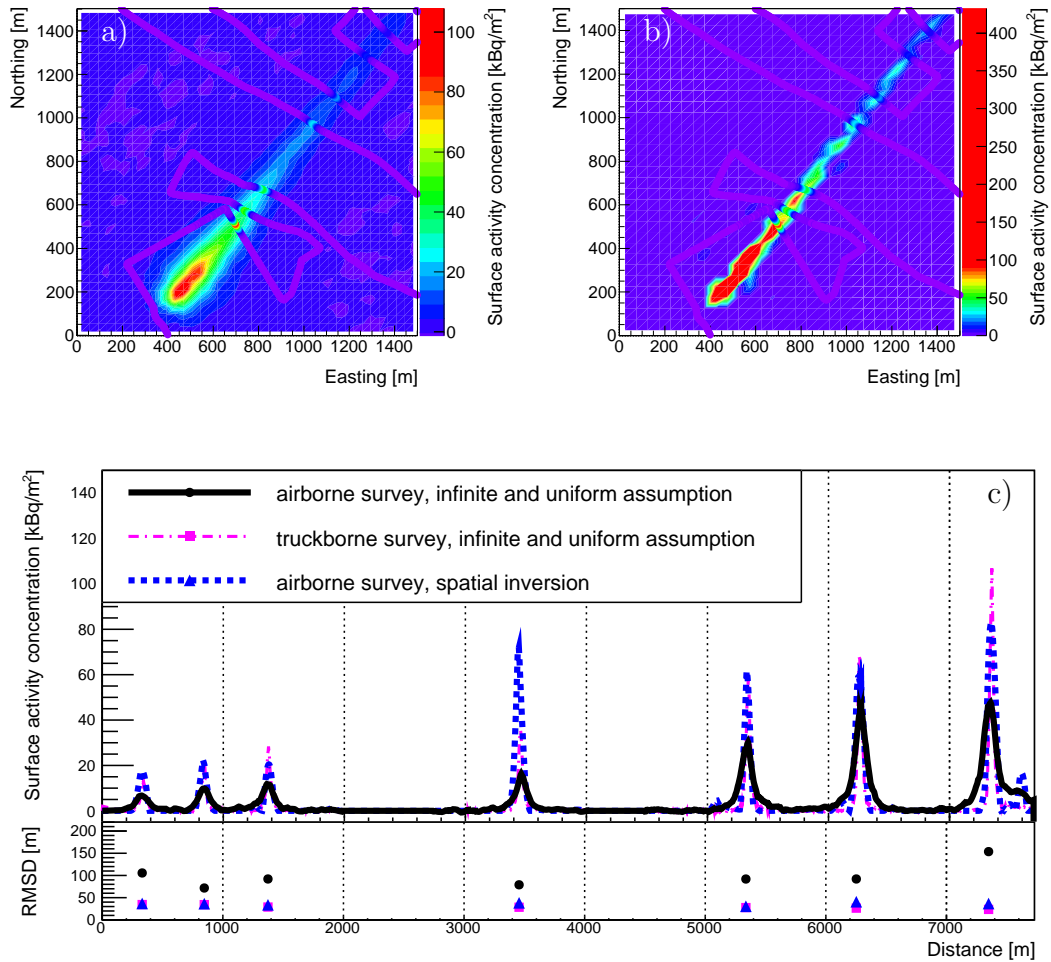


Figure 7: a) Aerial radiation survey following detonation of radiological dispersal device, with results of radiation survey from a truck-based system overlaid. b) Spatially deconvolved aerial radiation survey of the RDD fallout, with results of radiation survey from a truck-based system. Colour scale is the same in a) and b) and is optimized to show the range of values of the result from the truckborne survey. c) (top) Transects of the deposited RDD plume following the path of the truck-based survey system. The solid line shows the aerial survey result sampled at the truck location. The dot-dashed line shows the truckborne survey result and the dashed line shows the aerial survey result after spatial deconvolution sampled at the truck location. (bottom) Root-mean-square deviation of the seven transects versus the location of maximum concentration of each transect according to the truckborne survey. Circles show the aerial survey result, squares show the truckborne survey and triangles show the spatially deconvolved aerial survey result.